# 4342 | Cornering performance of rigid wheel in granular media using coarse-scale DEM models

Aidan Dickerson [a], Bohumir Jelinek [a,*], George L. Mason [a], Thomas Skorupa [b], Michael Cole [b], Jody D. Priddy [c]

[a] *Center for Advanced Vehicular Systems, Mississippi State University, Mississippi State, Mississippi, United States*

[b] *U.S. Army Combat Capabilities Development Command Ground Vehicle Systems Center, Warren, Michigan, United States*

[c] *U.S. Army Engineer Research and Development Center, Geotechnical and Structures Laboratory, Vicksburg, Mississippi, United States*

** Corresponding author: bj48@cavs.msstate.edu*

**A B S T R A C T**

Understanding interactions of wheels and tracks with granular media under variable loading conditions, including longitudinal and side slip, is critical for prediction of mobility for wheeled and tracked vehicles in off-road environments. The discrete element method (DEM) is routinely used for modeling interaction of soil with track and tires, but the method's accuracy needs to be better established.

In this work, two DEM models from the Generic EDEM Material Model (GEMM) database from Altair®'s EDEM™ software package, which were identified (Jelinek et al., 2025) as the best match to physical experiments, are used to calculate tractive performance of a rigid wheel in sand under braked, towed, and powered conditions with side slip. The simulations follow the experiments by Shinone et al. (2010), examining a 165/60R13 wheel with constant circumferential velocity of 97.6 mm/s and vertical contact load of 980 N operating in powered conditions under forward slips in the range of -5.9% to 54.8%. The steady-state tractive forces on the wheel in sand were evaluated under the same forward slip conditions as in the experiment, except with added side slip of 3, 6, and 12 degrees. The side-slip effects on net traction, gross traction, and sinkage of the wheel in sand are evaluated by comparison with forward-slip-only results, as well as analytical solutions for lateral forces. Lateral forces and overturning moments were then calculated and compared with relevant relationships derived from physical measurement and other simulation methods. The results indicate a good match to experimental trends, encouraging further use and calibration of the DEM soil-wheel interaction models.

*Keywords*
Off-road mobility
Tractive performance
Discrete element method
Rigid wheel
Side slip

## 1. Introduction

Prediction of vehicle mobility for vehicles in off-road environment presents a challenge for agriculture, construction, military, and space exploration. The subgrade materials that the off-road vehicle operates on may include rock, gravel, sand, silt, clay soil, or their mixtures with various degrees of saturation. DEM-based numerical models of soils provide truthful physical characterization of particulate nature of soil subgrade; however, due to large number of particles in fine grain soils, a compromise need to be found between sufficiently accurate representation of the particulate nature of the soil and capabilities of the high-performance computing.

Multiple studies have used DEM to characterize the interaction of granular subgrades with rigid wheels, nevertheless only a few of them include side slip. The tractive performance of off-road wheels on dry sand including steering was analyzed by Du et al. 2017a, 2017b, 2018. A DEM simulation along with comparison with analytical results were presented (Hu et al., 2021). These models, however, require careful calibration (Coetzee, 2017; Zeng et al., 2020a, 2020b), and, in many cases, non-spherical particles are used to better match the experiments (Coetzee, 2020).

This work presents recent progress on extension of our previous effort (Jelinek et al., 2025) to side slip. The goal is to assess capability of coarse grain DEM models to predict lateral forces and torques acting on a smooth wheel operating in dry sand under braked and powered conditions with side slip.

## 2. Discrete element method background

A particle bed to simulate wheel-soil interactions was generated using particle-factory functionality of the Altair®'s EDEM™ software. The particle bed was assembled from five identical material blocks repeated along the longitudinal direction. Only the particles in a single block were settled under periodic boundary conditions to lower the simulation time needed to populate the bed with particles. A smooth-surface cylindrical wheel without tread was constructed from triangular facets. Fig. 1 illustrates the wheel and enclosing box while Table 1 specifies their dimensions.

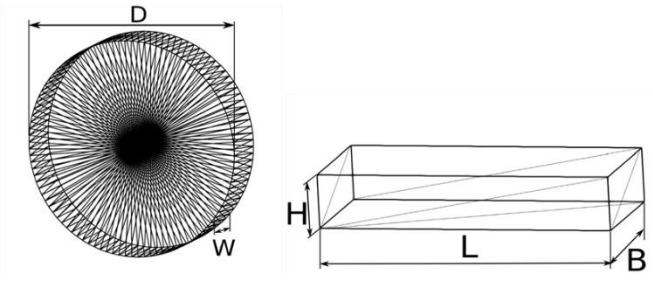


*Fig. 1. Triangular facet representation of the wheel and enclosing box*

*Table 1*
*Wheel and Box Dimensions*

| Property | Symbol | Value | Units |
|---|---|---|---|
| Wheel diameter | $D$ | 53.49 | cm |
| Wheel width | $W$ | 16.99 | cm |
| Wheel weight | $F_G$ | 980.33 | N |
| Box length | $L$ | 301.5 | cm |
| Box width | $B$ | 48.0 | cm |
| Box depth | $H$ | 60.5 | cm |
| Soil depth | $h$ | 60 | cm |
| Number of particles | $N$ | 97152 | - |

https://doi.org/10.56884/ABCD1234 *(ed. note: ISTVS will update your paper's DOI)*
ISBN 978-1-942112-58-7 

All particles have a multi-spherical shape. Individual spheres had a radius of 9.5mm with a fixed overlap. Fig. 2 visualizes the multi-sphere particles.

*Fig. 2. Multi-spherical particle shape*

The Hertz-Mindlin (no slip) and Hertz-Mindlin JKR (Johnson et al., 1971) models were used to represent DEM contact interactions. The GEMM database does not include material models with elasto-plastic properties such as Edinburgh Elastic-Plastic-Adhesive models (Jones, 2003; Jones et al., 2004; Thakur et al., 2014), nor Type C rolling friction models (Ai et al., 2011). Hertz-Mindlin (Mindlin and Deresiewicz, 1953) is the default model used in EDEM due to its accurate and efficient force calculation. The Hertz-Mindlin JKR model was used for particles with a non-zero JKR coefficient. For Hertz-Mindlin, the normal force is a function of normal overlap $\delta_n$:

$$F_n = \frac{4}{3} E^* \sqrt{R^*} \delta_n^{\frac{3}{2}} \tag{1}$$

where the $E^*$ is the equivalent Young's Modulus and $R^*$ is the equivalent radius. They are defined as:

$$\frac{1}{R^*} = \frac{1}{R_i} + \frac{1}{R_j} \tag{2}$$

$$\frac{1}{E^*} = \frac{\left(1 - v_i^2\right)}{E_i} + \frac{\left(1 - v_j^2\right)}{E_j} \tag{3}$$

with $E^i, v^i, R^i$, and $E^j, v^j, R^j$ being the Young's Modulus, Poisson ratio, and radius of each sphere in contact. Additionally, there is a damping force, $F_n{}^d$, given by:

$$\boldsymbol{F_n^d} = -2\sqrt{\frac{5}{6}}\beta\sqrt{S_n m^*}\,\boldsymbol{v_n^{rel}} \tag{4}$$

$$m^* = \left(\frac{1}{m_j} + \frac{1}{m_i}\right)^{-1} \tag{5}$$

$$\beta = \frac{-\ln e}{\sqrt{ln^2 e + \pi^2}} \tag{6}$$

$$S_n = 2E^*\sqrt{R^*\delta_n} \tag{7}$$

where m* is the equivalent mass, $\boldsymbol{v_n^{rel}}$ is the normal component of the relative velocity, $\beta$, and $S_n$ (the normal stiffness). The constant $e$ is the coefficient of restitution, the tangential force, $F_t$, depends on the tangential overlap $\delta_t$ and the tangential stiffness $S_t$.

$$F_t = -S_t \delta_t \tag{8}$$

$$S_t = 8G^*\sqrt{R^*\delta_n} \tag{9}$$

Here, $G^*$ is the equivalent shear modulus. Additionally, tangential damping is defined as:

$$\boldsymbol{F_t^d} = -2\sqrt{\frac{5}{6}}\beta\sqrt{S_t m^*}\,\boldsymbol{v_t^{rel}} \tag{10}$$

where $\boldsymbol{v_t^{rel}}$ is the relative tangential velocity. The tangential force is limited by Coulomb friction, $\mu_s F_n$, where $\mu_s$ is the coefficient of static friction. The rolling friction (Sakaguchi et al., 1993) is implemented by applying torque

$$\tau_i = -\mu_r F_n d_i \Omega_i \tag{11}$$

to the contacting objects, where $\mu_r$ is the coefficient of rolling friction, $d_i$ is the distance of the $i$-th contact point from the center of mass and $\Omega_i$ is the unit angular velocity vector of the object at the contact point.

The Hertz-Mindlin contact model with JKR cohesion (Johnson et al., 1971) allows modelling of cohesive materials. It calculates the normal force as a function of overlap $\delta_n$ and the surface energy parameter γ as follows:

$$F_{JKR} = -4\sqrt{\pi\gamma E^*}a^{3/2} + \frac{4E^*}{3R^*}a^3 \tag{12}$$

$$\delta_n = \frac{a^2}{R^*} - \sqrt{\frac{4\pi\gamma a}{E^*}} \tag{13}$$

where $E^*$ is the equivalent Young modulus, $a$ is contact overlap radius, and $R^*$ is the equivalent radius from Eq. 2. Wheel slip and circumferential velocity were used as an initial condition to each system. Wheel slip is defined as:

$$i = 1 - \frac{v_f}{\omega r} \tag{14}$$

Equation 14 defines $i$ as wheel slip in terms of the wheel forward velocity $v_f$, wheel angular speed $\omega$, and the wheel radius $r=D/2$. Post-processing values such as net traction and gross traction were calculated using Eq. 15 and 16 respectively. Sinkage amount was based on the initial position of the suspended wheel.

$$F^x = \sum_j F_j^x \tag{15}$$

$$T = \sum_j F_j^t d_j \tag{16}$$

$F^x$ is the forward component of the contact force, $F^t$ is the wheel-surface-tangential component of the contact force, $D$ is the wheel diameter and $d_j$ is the distance from the contact point to the wheel axis. $F^t$ has negative/positive sign if the force acts to increase/decrease wheel rotation.

DEM nomenclature is summarized in Section 7.

*Table 2*
*Particle properties for two DEM models selected from GEMM database due to their best match to measurements from Shinone et al. (2010).*

| DEM Mat. # | $\nu$ | $\rho$ | $G$ | $e^p$ | $\mu_s{}^p$ | $\mu_r{}^p$ | $\gamma^p$ | $e^g$ | $\mu_s{}^g$ | $\mu_r{}^g$ | $\gamma^g$ |
|---|---|---|---|---|---|---|---|---|---|---|---|
| 1311 | 0.25 | 3300 | 10 | 0.55 | 0.68 | 0 | 0 | 0.5 | 0.45 | 0.15 | 0 |

| | | | | | | | | | | | |
|---|---|---|---|---|---|---|---|---|---|---|---|
| 1111 | 0.25 | 3300 | 10 | 0.55 | 0.44 | 0 | 0 | 0.5 | 0.45 | 0.15 | 0 |

*a superscript of *p* implies particle-particle interaction while *g* is a particle-geometry interaction

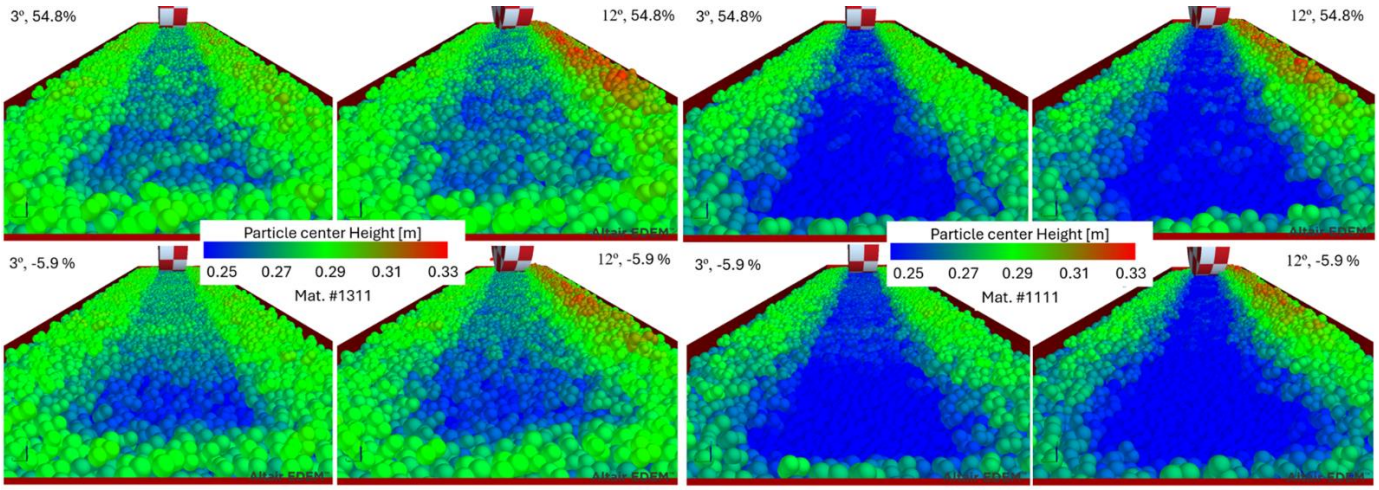


*Fig. 3 Final configurations of the wheel at 54.8% slip (upper row) and -5.9% slip (lower row) with 3° (odd columns) and 12° (even columns) side slip and particle bed material # 1311 (left half) and 1111 (right half).*

## 3. DEM material model selection

In Jelinek et al. (2025), ten DEM models from the GEMM database were selected and evaluated for their ability to match the experimental measurement of tractive performance of a wheel in dry sand performed by Shinone et al. (2010). GEMM database provides three selection criteria to select models with desired material properties. These are 1) particle size, 2) bulk density, and 3) an angle of repose. To match material characterization of the dry sand, the following material-selection criteria were applied in Jelinek et al. (2025): 1) the smallest available particle size, 2) a bulk density range of 1500-2000 kg/m$^3$, and 3) an angle of repose of 34°. Given these three selection criteria, the GEMM database returns ten materials. The evaluation in Jelinek et al. (2025) found that two out these ten materials, the DEM models with GEMM reference numbers 1311 and 1111, resulted in the closest match to tractive performance measurements by Shinone et al. (2010). These two materials differ only in a coefficient of static friction, and, similarly to dry sand, they don't exhibit a significant cohesion. They were selected in the present study for further evaluation of their ability to predict tractive performance of a wheel with side slip. The present study did not perform any direct calibration of the DEM materials, but instead selected the two materials with the best match (Jelinek et al. 2025) to forward-slip-only tractive performance measurements performed by Shinone et al. (2010).

## 4. Simulation results

The DEM simulation procedure follows the experiment by Shinone et al. (2010), with only difference being that side slip angles of 3°, 6°, and 12° were prescribed. Final configurations of the wheel from simulations at -5.9% and 54.8% forward slip with 3° and 12° side slips for the two materials are shown in Fig. 3. It is evident that material number 1111 with lower static friction coefficient resulted in higher wheel sinkage than material 1311 with higher static friction coefficient.

### *4.1. Side slip effects*

Fig. 4 compares drawbar pull ($F_x$), gross tractive effort ($M_y$/R) and sinkage results for materials 1311 and 1111 at varying side slip. *X*-axis of the coordinate system points forward, *y* points left, and *z* points up. The forward component of the drawbar pull $F_x$ decreases with increased side slip. Material 1111, with static friction lower than material 1311, produces less forward pull and more sinkage at each side slip. Interestingly, gross tractive effort is higher for lower-friction material 1111, pointing out even higher losses when wheel operates with higher sinkage. The most significant difference in all three variables is seen when the side slip changes from 6° and 12°.

Fig. 5 compares lateral force ($F_y$), overturning moment ($M_x$/R) and self-aligning moment ($M_z$/R) for the two materials. Side slip force $F_y$ increases with side slip angle, as expected. The same is true for the magnitude of overturning torque $M_x$ and for self-aligning torque $M_y$, with self-aligning torque having much lower value than overturning torque. A significant change is seen in all three variables even when the side slip changes from 0° to 3°.

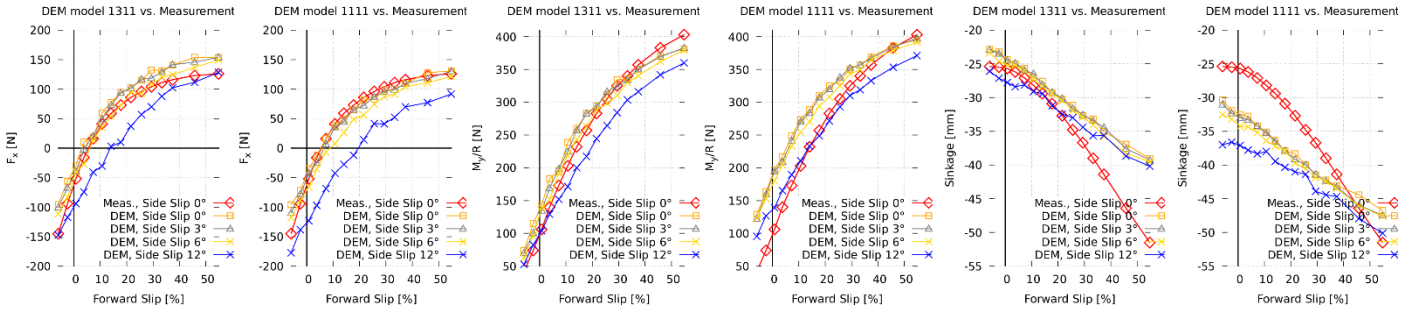


*Fig. 4 Drawbar pull, gross tractive effort, and sinkage from DEM models 1311 and 1111 at varying side slip, along with measurement values at zero side slip.*

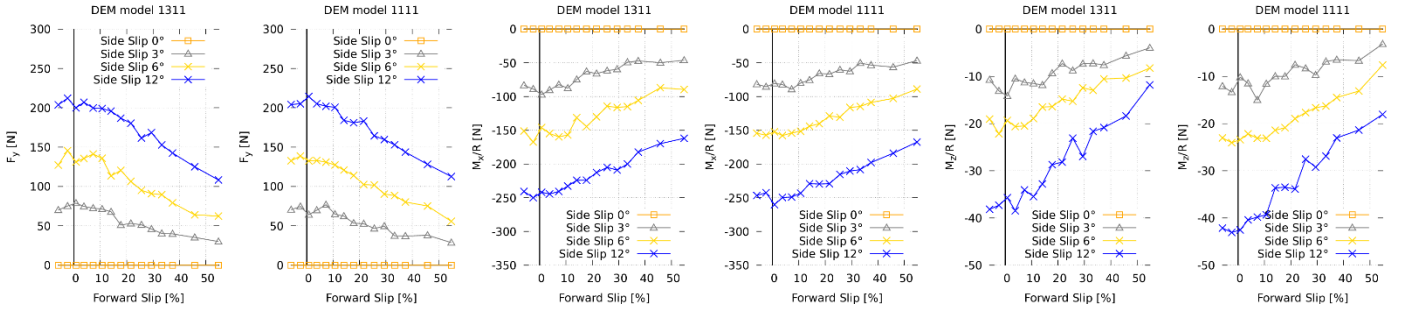


*Fig. 5 DEM simulation results for lateral force, self-aligning torque, and overturning torque for varying side slip, showing increase in magnitude with increasing side slip as expected.*

### *4.2. Stress profiles and relative velocities along the wheel-soil contact patch*

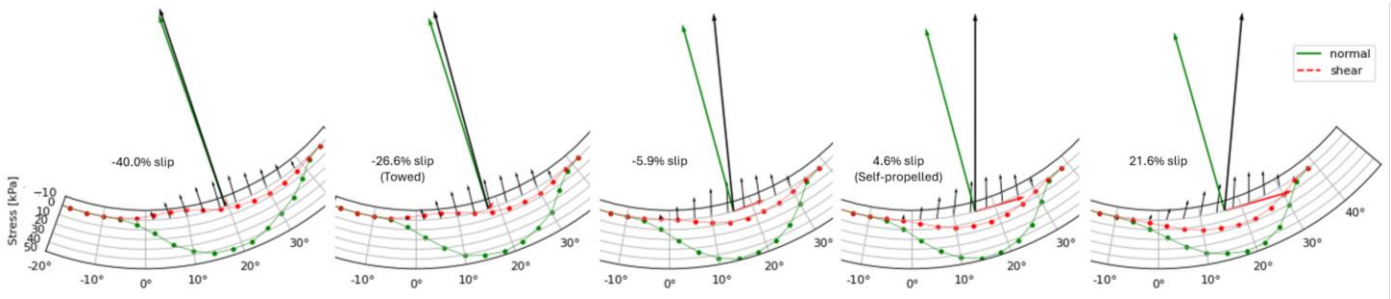


*Fig. 6 Normal and shear stress profiles along the wheel-soil contact patch for straight-driving wheel in DEM material 1111*

Fig. 6 shows normal and sheer stress profiles along the wheel-circumference contact with soil for three prescribed slips (-40%, -5.9%, and 21.6%) by forcing decreasing forward velocities and keeping the circumferential wheel velocity of $v_c$=0.0976 m/s (Shinone et al. 2010), towed (forcing $v_x$ with the value of $v_c$), and self-propelled (prescribed $v_c$=0.0976 m/s). With prescribed slip, the wheel is only allowed to move freely in vertical ($z$) direction. Towed and self-propelled conditions allow one extra degree of freedom: free angular velocity $\omega_y$ in towed, and free horizontal velocity $v_x$ in self-propelled conditions. The largest black arrow in Fig. 6 shows the total force exerted by soil subgrade on the wheel. Its vertical component balances the wheel weight, which is 980 N. The green arrow shows the sum of normal forces, and the red arrow the sum of shear forces exerted by soil on the wheel.

Relative velocity of soil particles at the wheel-soil contact surface with respect to wheel circumference is shown in Fig. 7. The transition from negative to positive shear stress roughly corresponds to the transition from negative to positive relative shear velocity of particles with respect to the wheel surface. Entry and exit angles were estimated by approximating the normal stress profile with a squared "tilted" sine function shown in Equations (17) and (18).

$$\tau(\theta') = \left(\frac{1}{t}\arctan\left(\frac{t\sin(\theta'-\pi)}{1-t\cos(\theta'-\pi)}\right)\right)^2 \quad (17)$$

where $\theta'$ is

$$\theta' = \pi(\theta-\theta_2)/(\theta_1-\theta_2) \quad (18)$$

Here, $\theta_1$ and $\theta_2$ are the angles at which the wheel enters and exits the soil. The approximation in Equations (17) and (18) offers an alternative to connected halves of Gaussian distributions used by

https://doi.org/10.56884/ABCD1234 *(ed. note: ISTVS will update your paper's DOI)*
ISBN 978-1-942112-58-7 

Horiko and Ishigami (2020). The shear stress profile in Fig. 6 resembles those measured by Horiko and Ishigami (2020), however the shear stress transition point in the present study does not correspond the location of maximum normal stress. Fig. 8 shows maximum normal stress value along with entry angle, exit angle, and angle of maximum normal stress angle at varying slips. Interestingly, the present study show a minimum in the dependence of the entry angle on slip, while Wong and Reece (1967) show increasing trend only. The maximum normal stress being largest close to zero slips can be justified by contact patch being shortened at close-to-zero slips, as indicated by lower difference between the entry and exit angle for close-to-zero slips.

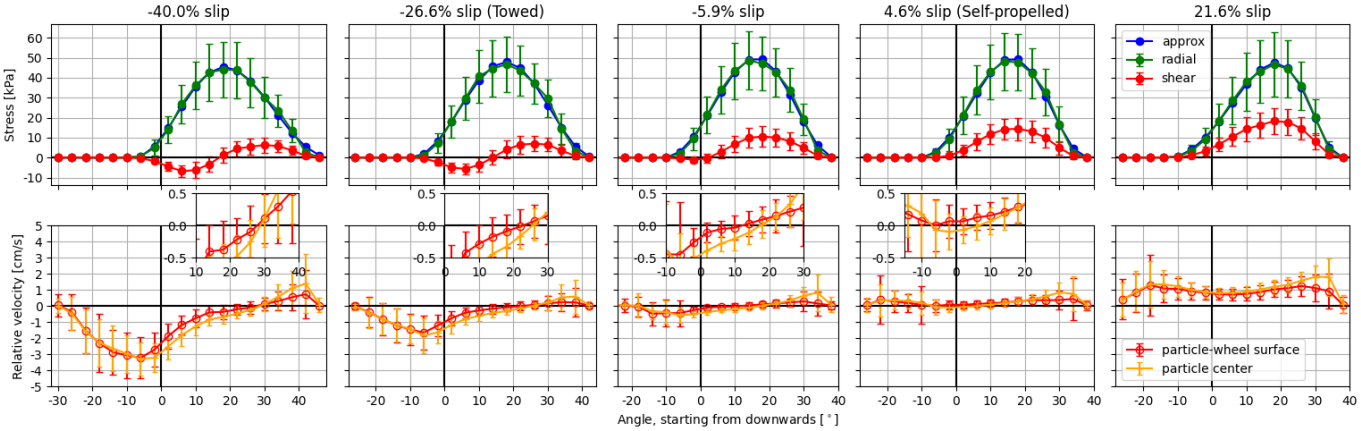


*Fig. 7 Velocity of particles relative to the wheel circumference at the particle centers and at the contact point (lower row) aligned with normal and shear stress profiles along the contact patch (upper row).*

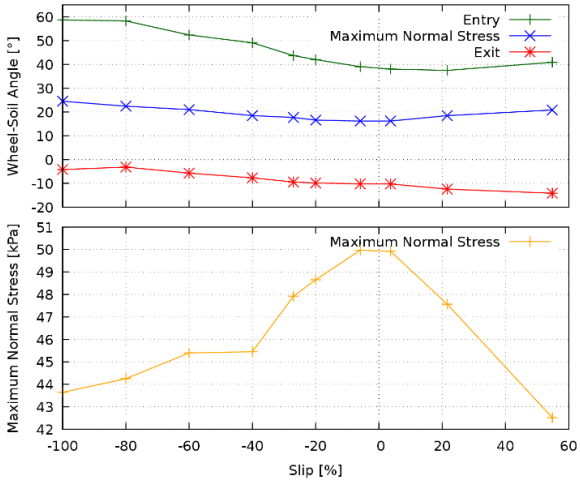


*Fig. 8 Maximum normal stress values along with entry angle, exit angle, and maximum normal stress angle at varying slips.*

Fig. 9 shows average particle-center velocities under the wheel. The forward velocity of the wheel at each slip is indicated by the topmost black arrow. The rim velocity is indicated by three arrows: first on the left side of the rim, second on the right slide of the rim, and the velocity of the bottom-most point of the rim is indicated by an arrow placed between just above the bottom-most point of the rim. It is important to note that velocities of soil particles were averaged over multiple steps of the simulation. The averaging started 7 seconds after the wheel started moving forward to allow the wheel-soil system to reach a steady state and finished when the wheel center reached the distance of 1 meter from the center of the box, what is approximately 0.5 meter away from the end of the box to avoid effects of box ending wall.

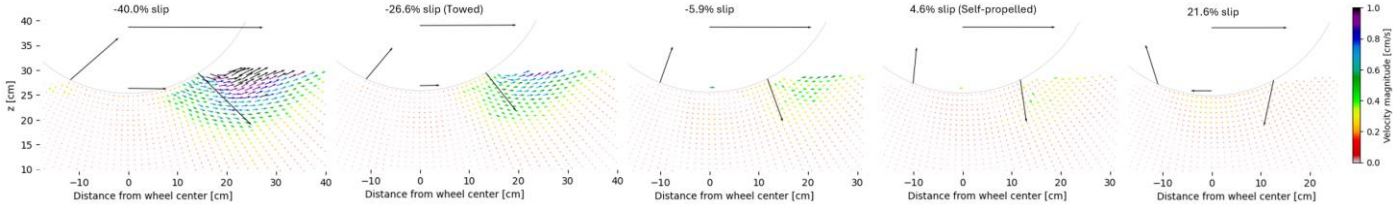


*Fig. 9 Averaged particle velocities under the wheel. Forward and wheel surface velocities are shown as large black arrows*

## 5. Comparison with analytical expressions

To help analyze the results of the simulation and evaluate their accuracy, an analytical model of tractive performance was created using a combination of the Bekker and Janosi terramechanics models (Bekker, 1956; Janosi and Hanamoto, 1961). The Bekker model is used to evaluate sinkage, while the Janosi model is used for evaluating drawbar pull and gross tractive effort. The equations used for this analytical solution are derived from previous work (Hu et al., 2021; Li and Bingham, 2022).

$$\sigma_{Bekker} = \left(\frac{k_c}{b} + k_\varphi\right) * |z|^n \quad (19)$$

$$z_{equillibrium} = P + Q - \sigma * A_{modified} \quad (20)$$

$$A_{modified} = \sqrt{2 * r * |z| - |z|^2} * b * \cos(\beta) * (1 - i)^\alpha \quad (21)$$

$$Q = D * i * e^{-E*i} * P \quad (22)$$

Equations 19, 20, 21 and 22 above represent the normal stress $\sigma_{Bekker}$, the sinkage equilibrium, the modified contact area, and a load mimicking the bulldozing effect, respectively. Table 3 below defines the parameters used in these equations.

*Table 3*
*Nomenclature for Bekker / Janosi terramechanics models*

| Symbol | Definition | Units |
|---|---|---|
| $z$ | Sinkage | [m] |
| $b$ | Wheel width | [m] |
| $k_c$ | Cohesive modulus | [N/m$^{n+1}$] |
| $k_\varphi$ | Friction modulus | [N/m$^{n+2}$] |
| $\sigma$ | Normal stress, Bekker | [Pa] |
| $P$ | Load | [Pa] |
| $Q$ | Additional load from bulldozing effect | [Pa] |
| $r$ | Wheel radius | [m] |
| $\beta$ | Side-slip angle | [rad] |
| $i$ | Forward slip | [] |
| $D$ | Additional load scaling parameter | [] |
| $E$ | Shear scaling for additional load | [] |
| $n$ | Bekker exponent | [] |
| $c$ | Soil cohesion | [Pa] |
| $\varphi$ | Internal friction angle | [rad] |
| $K_x$ | Longitudinal shear modulus | [m] |
| $K_y$ | Lateral shear modulus | [m] |
| $\mu_{rr}$ | Running resistance friction | [] |
| $\alpha$ | Slip exponent | [] |
| $A$ | Contact area | [m$^2$] |

The above parameters constitute the Bekker and Janosi soil characterization along with units for calculation in their corresponding equations. Some parameters, such as sinkage, are converted to other units after calculation to improve clarity in displaying their results.

$$\tau_x = (c + \sigma_{Bekker} * \tan(\varphi)) * \left(1 - e^{-\frac{r*i}{K_x}}\right) \quad (23)$$

$$\tau_y = (c + \sigma_{Bekker} * \tan(\varphi)) * \left(1 - e^{-\frac{|r*\tan(\beta)|}{K_y}}\right) \quad (24)$$

$$DBP = A_{modified} * (\tau_x * \cos(\beta) - \tau_y * \sin(\beta)) \quad (25)$$

Equations 23, 24, and 25 show how the shear stresses in each direction are calculated, then the calculation of the drawbar pull.

$$RR = P * \mu_{rr} \quad (26)$$

$$GTE = DBP + RR \quad (27)$$

Equations 26 and 27 above show how to calculate running resistance and gross tractive effort, respectively. Together, each of these equations can be used to generate an analytical solution for the effects of side slip.

The fitting of DEM results to Bekker / Janosi parameters was done by using a Python script utilizing several tools from the SciPy library, which is a library focused on scientific work with extensive functionality for solving complex systems of equations. The issue when using these calculations is that some of the necessary parameters are not included in the reference material from Shinone et al. (2010) on which the original work involving only forward slip was based. To compensate for this, SciPy tools such as *fsolve*, *least squares*, and *differential evolution* were used to fit the solution to Shinone et al. (2010) data using a 0° side-slip angle. That provided approximations for the missing parameters through several stages of fitting. Documentation of these tools can be found on SciPy's website ("SciPy User Guide," 2025).

Example results of fitting results from simulations of the DEM material number 1311 with 12° side slip to Bekker / Janosi soil model are shown in Fig. 10Fig. 11, and Fig. 12, demonstrating a very good fit for the drawbar pull and gross traction and a reasonable fit for sinkage. Bekker and Janosi parameters obtained by fitting 12° side slip response from both 1311 and 1111 DEM materials are listed in Table 4.

*Table 4*
*Bekker and Janosi parameters fitted to DEM results mat. # 1311 and 1111*

| Parameter | Mat. # 1311 | Mat. # 1111 | Units |
|---|---|---|---|
| $k_c$ | 1.40 | 1.20 | [N/m$^{n+1}$] |
| $k_\varphi$ | 9,920 | 31,500 | [kN/m$^{n+2}$] |
| $n$ | 1.48 | 2.00 | [] |
| $K_x$ | 0.164 | 0.206 | [m] |
| $K_y$ | 0.00124 | 0.00147 | [m] |
| $D$ | 0.703 | 0.240 | [m] |
| $E$ | 1.00 | 1.00 | [] |
| $\mu_{rr}$ | 0.207 | 0.255 | [] |
| $\alpha$ | 0.684 | 0.869 | [] |

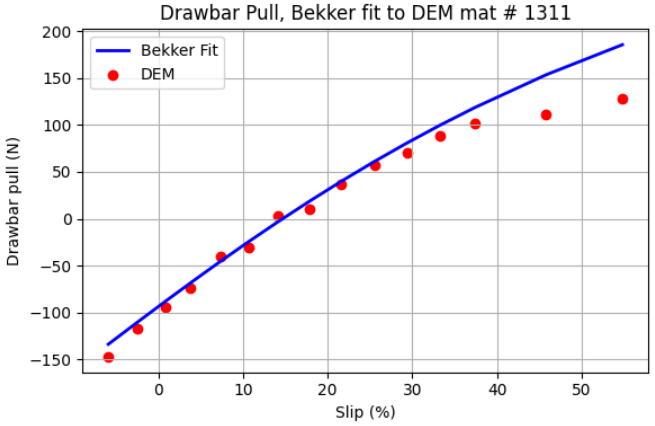


*Fig. 10 Drawbar pull- Bekker / Janosi fit to DEM material # 1311*

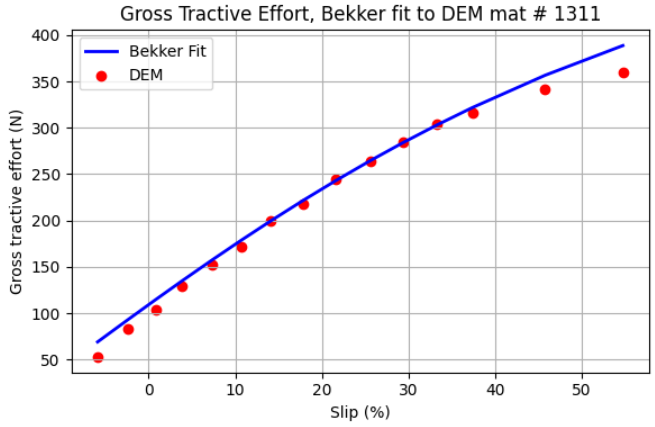


*Fig. 11 Gross tractive effort - Bekker / Janosi fit to DEM material # 1311*

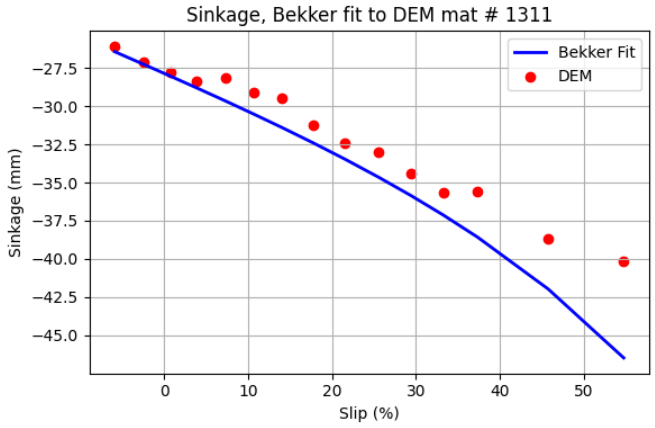


*Fig. 12 Sinkage – Bekker / Janosi fit to DEM material # 1311*

## 6. Conclusions and future work

This work analyzes the results of DEM simulations including side slip. A new approximation of the normal stress profile along the wheel-soil contact patch for a straight-driving wheel is proposed. The results were fitted to Bekker / Janosi terramechanics relations. A reasonable agreement with Bekker theory is found.

In the future, further calibration of DEM material parameters can be performed to better match the experimental data. It would add value significantly if the side slip results were compared and additionally calibrated with an experiment. Approximation for the shear stress profile, allowing to predict drawbar pull and gross traction, will be investigated.

## 7. Nomenclature

| | | |
|---|---|---|
| $a$ | Contact radius | [m] |
| $B$ | Box width | [m] |
| $D$ | Wheel diameter | [m] |
| $d_i$ | Distance from the i-th contact point from the center of mass | [m] |
| $d_j$ | Distance from the j-th particle wheel contact point to wheel axis | [m] |
| $e$ | Coefficient of restitution | [] |
| $E$ | Young's modulus | [m] |
| $F^d$ | Damping force | [m] |
| $F_G$ | Wheel weight | [N] |
| $F_t$ | Tangent component of contact force | [N] |
| $F_n$ | Normal component of contact force | [N] |
| $F^x$ | Forward component of force on wheel | [N] |
| $G$ | Shear modulus | [MPa] |
| $H$ | Box depth | [m] |
| $h$ | Soil depth | [m] |
| $i$ | Wheel slip | [] |
| $L$ | Box length | [m] |
| $m$ | Mass | [kg] |
| $N$ | Number of particles | [] |
| $R$ | Hertz-Mindlin radius | [m] |
| $R_i$ | Radius of sphere in contact | [m] |
| $S$ | Stiffness | [N/m] |
| $T$ | Gross tractive effort | [Nm] |
| $t$ | Parameter of the normal stress approximation function | [] |
| $v_f$ | Forward component of wheel velocity | [m/s] |
| $v_n^{rel}$ | Relative normal velocity | [m/s] |
| $v_t^{rel}$ | Relative tangential velocity | [m/s] |
| $W$ | Wheel width | [m] |
| $\alpha$ | Contact overlap | [m] |
| $\beta$ | Damping ratio | [] |
| $\gamma$ | JKR surface energy parameter | [J/m$^2$] |
| $\delta$ | Overlap | [m] |
| $\mu$ | Coefficient of friction | [] |
| $\mu_r$ | Coefficient of rolling friction | [] |
| $\mu_s$ | Coefficient of static friction | [] |
| $\nu$ | Poisson's ratio | [] |
| $\rho$ | Solid Density (material without voids) | [kg/m$^3$] |
| $\omega$ | Angular speed | [rad/s] |
| $\tau_i$ | Rolling friction torque for i-th contact | [Nm] |

## 8. Acknowledgements

This material is based upon research conducted under contract W912HZ-22-C0004 with the U.S. Army Engineer Research and Development Center (ERDC). The views and conclusions contained herein are those of the authors and should not be interpreted as necessarily representing the official policies or endorsements, either expressed or implied, of ERDC or the U.S. Government.

## 9. Declaration of competing interest

The authors declare that they have no known competing financial interests or personal relationships that could have appeared to influence the work reported in this paper.

## 10. References

Ai, J., Chen, J.-F., Rotter, J.M., Ooi, J.Y., 2011. Assessment of rolling resistance models in discrete element simulations. Powder Technology 206, 269–282. https://doi.org/10.1016/j.powtec.2010.09.030

Bekker, M.G., 1956. Theory of Land Locomotion: The Mechanics of Vehicle Mobility, 9690401st ed. University of Michigan Press, Ann Arbor, MI. https://doi.org/10.3998/mpub.9690401

Coetzee, C., 2020. Calibration of the discrete element method: Strategies for spherical and non-spherical particles. Powder Technology 364, 851–878. https://doi.org/10.1016/j.powtec.2020.01.076

Coetzee, C.J., 2017. Review: Calibration of the discrete element method. Powder Technology 310, 104–142. https://doi.org/10.1016/j.powtec.2017.01.015

Du, Y., Gao, J., Jiang, L., Zhang, Y., 2018. Development and numerical validation of an improved prediction model for wheel-soil interaction under multiple operating conditions. Journal of Terramechanics 79, 1–21.

Du, Y., Gao, J., Jiang, L., Zhang, Y., 2017a. Numerical analysis on tractive performance of off-road wheel steering on sand using discrete element method. Journal of Terramechanics 71, 25–43.

Du, Y., Gao, J., Jiang, L., Zhang, Y., 2017b. Numerical analysis of lug effects on tractive performance of off-road wheel by DEM. Journal of the Brazilian Society of Mechanical Sciences and Engineering 39, 1977–1987.

Horiko, S., Ishigami, G., 2020. Experimental study on wheel-soil interaction mechanics using in-wheel sensor and particle image velocimetry part II. Analysis and modeling of shear stress of lightweight wheeled vehicle. Journal of Terramechanics 91, 243–256. https://doi.org/10.1016/j.jterra.2020.07.002

Hu, C., Gao, J., Song, X., Zhang, M., Tan, X., 2021. Analytical modeling and DEM analysis of soil–wheel interaction under cornering and skidding conditions in off-road vehicles. AIP Advances 11, 085122. https://doi.org/10.1063/5.0057046

Janosi, Z., Hanamoto, B., 1961. The analytical determination of drawbar pull as a function of slip for tracked vehicles in deformable soils, in: International Society for Terrain-Vehicle Systems, 1st Int. Conf.

Jelinek, B., Card, A., Mason, G.L., Grebner, K., Dickerson, A., Skorupa, T., Cole, M., Priddy, J.D., 2025. Tractive performance of rigid wheel in granular media using coarse-scale DEM models. Journal of Terramechanics 117, 101016. https://doi.org/10.1016/j.jterra.2024.101016

Johnson, K.L., Kendall, K., Roberts, A.D., 1971. Surface energy and the contact of elastic solids. Proc. R. Soc. Lond. A 324, 301–313. https://doi.org/10.1098/rspa.1971.0141

Jones, R., 2003. From Single Particle AFM Studies of Adhesion and Friction to Bulk Flow: Forging the Links. Granular Matter 4, 191–204. https://doi.org/10.1007/s10035-002-0122-6

Jones, R., Pollock, H.M., Geldart, D., Verlinden-Luts, A., 2004. Frictional forces between cohesive powder particles studied by AFM. Ultramicroscopy 100, 59–78. https://doi.org/10.1016/j.ultramic.2004.01.009

Li, Z.Q., Bingham, L.K., 2022. NASA White Paper - Terramechanics for LTV Modeling and Simulation.

Mindlin, R.D., Deresiewicz, H., 1953. Elastic Spheres in Contact Under Varying Oblique Forces. Journal of Applied Mechanics 20, 327–344. https://doi.org/10.1115/1.4010702

Sakaguchi, H., Ozaki, E., Igarashi, T., 1993. Plugging of the Flow of Granular Materials during the Discharge from a Silo. International Journal of Modern Physics B 07, 1949–1963. https://doi.org/10.1142/S0217979293002705

SciPy User Guide [WWW Document], 2025. URL https://docs.scipy.org/doc/scipy/tutorial/index.html

Shinone, H., Nakashima, H., Takatsu, Y., Kasetani, T., Matsukawa, H., Shimizu, H., Miyasaka, J., Ohdoi, K., 2010. Experimental Analysis of Tread Pattern Effects on Tire Tractive Performance on Sand using an Indoor Traction Measurement System with Forced-slip Mechanism. Engineering in Agriculture, Environment and Food 3, 61–66. https://doi.org/10.1016/S1881-8366(10)80020-5

Thakur, S.C., Morrissey, J.P., Sun, J., Chen, J.F., Ooi, J.Y., 2014. Micromechanical analysis of cohesive granular materials using the discrete element method with an adhesive elasto-plastic contact model. Granular Matter 16, 383–400. https://doi.org/10.1007/s10035-014-0506-4

Wong, J.-Y., Reece, A.R., 1967. Prediction of rigid wheel performance based on the analysis of soil-wheel stresses part I. Performance of driven rigid wheels. Journal of Terramechanics 4, 81–98.

Zeng, H., Xu, W., Zang, M., Yang, P., 2020a. Calibration of DEM-FEM model parameters for traction performance analysis of an off-road tire on gravel terrain. Powder Technology 362, 350–361. https://doi.org/10.1016/j.powtec.2019.12.006

Zeng, H., Xu, W., Zang, M., Yang, P., Guo, X., 2020b. Calibration and validation of DEM-FEM model parameters using upscaled particles based on physical experiments and simulations. Advanced Powder Technology 31, 3947–3959. https://doi.org/10.1016/j.apt.2020.06.044